PROCEEDINGS A

royalsocietypublishing.org/journal/rspa

Research

Cite this article: Zheng Y, Niloy I, Tobasco I, Celli P, Plucinsky P. 2023 Modelling planar kirigami metamaterials as generalized elastic continua. *Proc. R. Soc. A* **479**: 20220665. https://doi.org/10.1098/rspa.2022.0665

Received: 13 October 2022
Accepted: 1 March 2023

Subject Areas:
mechanics, mechanical engineering

Keywords:
metamaterials, kirigami, continuum modelling, finite-element method

Author for correspondence:
P. Plucinsky
e-mail: plucinsk@usc.edu

Modelling planar kirigami metamaterials as generalized elastic continua

Y. Zheng[1], I. Niloy[2], I. Tobasco[3], P. Celli[2] and P. Plucinsky[1]

[1]Aerospace and Mechanical Engineering, University of Southern California, Los Angeles, CA 90089, USA
[2]Civil Engineering, Stony Brook University, Stony Brook, NY 11794, USA
[3]Mathematics, Statistics, and Computer Science, University of Illinois Chicago, Chicago, IL 60607, USA

IT, 0000-0003-3618-8036; PP, 0000-0003-2060-8657

Kirigami metamaterials dramatically change their shape through a coordinated motion of nearly rigid panels and flexible slits. Here, we study a model system for mechanism-based planar kirigami featuring periodic patterns of quadrilateral panels and rhombi slits, with the goal of predicting their engineering scale response to a broad range of loads. We develop a generalized continuum model based on the kirigami's effective (cell-averaged) nonlinear deformation, along with its slit actuation and gradients thereof. The model accounts for three sources of elasticity: a strong preference for the effective fields to match those of a local mechanism, inter-panel stresses arising from gradients in slit actuation, and distributed hinge bending. We provide a finite-element formulation of this model and implement it using the commercial software Abaqus. Simulations of the model agree quantitatively with experiments across designs and loading conditions.

1. Introduction

Mechanical metamaterials are solids whose global response is dominated by geometry and topology, rather than material physics. A typical mechanical metamaterial, like the Miura-Origami [1] or the rotating-squares lattice [2], is built from a pattern of repeating unit cells. Each cell is composed of stiff and flexible elements, whose layout enables for a bulk shape-morphing

THE ROYAL SOCIETY
PUBLISHING

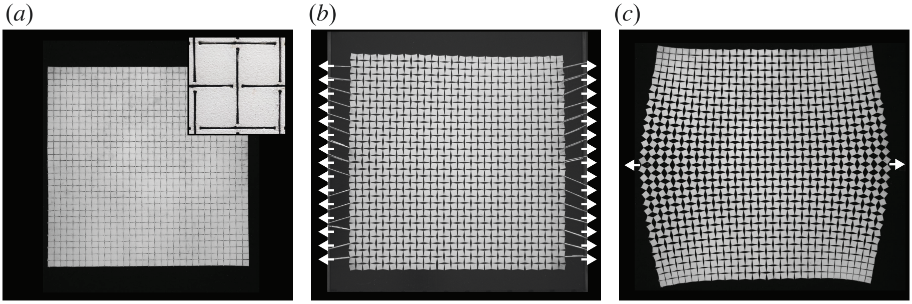

Figure 1. (*a*) Rotating-squares mechanical metamaterial in its undeformed configuration. (*b*) Uniform response of the metamaterial to homogeneous loading. (*c*) Non-uniform, locally mechanistic response to inhomogeneous loading.

response to stimuli. The geometric rules linking design to deformation in such systems have captivated theorists [3–5]. In parallel, the embrace of shape-morphing in modern engineering—for the design of stents [6,7], soft robotic grippers [8,9], deployable space structures [10,11] and the like—has drawn applied researchers to these systems in an effort to demonstrate new functionalities. Thus, mechanical metamaterials sit at the intersection of engineering design and mechanics, where new paradigms are needed to realize their full potential.

This paper concerns one such paradigm, namely, how to best model the engineering scale response of a shape-morphing mechanical metamaterial under a broad range of loads. To illustrate the challenges, consider the example in figure 1. The pattern, a rotating-squares architecture, is composed of a repeating unit cell of four quadrilateral panels, shown in figure 1*a*. This design exhibits a single *mechanism* [2], which counter-rotates the panels periodically and results in an effectively uniform overall motion in response to homogeneous loads (figure 1*b*). However, when subjected to inhomogeneous loads (figure 1*c*), the slits actuate in a non-uniform way—one that is *locally mechanistic* rather than globally so—reflecting the interaction between the design of the unit cell and the choice of applied loads.

Behind this response is a complex interplay between geometry and elasticity. Two modelling approaches are common in the literature, the first of which is purely geometric: panels are taken to be rigid and connected by ideal hinges (folds, in origami), with the goal of characterizing rigid deformations and mechanisms using kinematic compatibility. This approach, first popularized in the origami literature [12–14], has rationalized the design of mechanical metamaterials and illuminated their basic mechanisms [15–22]. However, it does not include elasticity.

The second modelling approach is based on long-established structural mechanics ideas [23,24] exemplified in recent literature by the bar-hinge method [25,26] and related spring methods [27,28]. This approach replaces the metamaterial with assemblies of bars and hinges, whose geometric arrangement encodes desired morphing attributes. Elasticity is accounted for by modelling bars/hinges as linear/torsional springs, and the structure's response is analysed using standard numerical methods. While this approach is versatile and convenient for systems composed of a small number of building blocks, it can become computationally expensive for larger systems with many unit cells. Additionally, fitting spring stiffnesses to yield accurate global behaviours can be challenging.

Recently, a third approach has emerged from the idea of finding effective, coarse-grained models for the deformations of origami and kirigami [29–35]. In this approach, the metamaterial is modelled as an effectively continuum object, with the aim of capturing the collective response of its cells through averaging. Supporting this idea is the heuristic that origami and kirigami have many *soft modes*, as in figure 1*c*, that resemble mechanisms locally but describe global, non-mechanistic shape change. Focusing on kirigami, we highlight the works [28,32,34] which

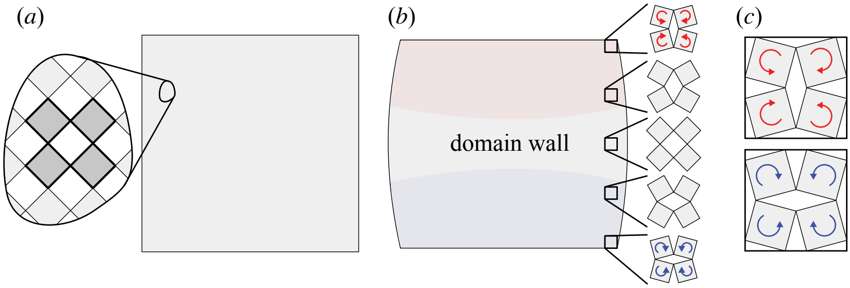

Figure 2. Example of 'micro'-incompatibilities, inspired by Deng *et al*. [28]. (*a*) The reference configuration is the open state of a rotating-squares pattern. (*b*) Forcing the pattern into opposite 'red' and 'blue' phases at the top and bottom leads to a domain wall. (*c*) Incompatible microstructures can have the same cell-averaged response.

are closest to what we do here. The works of Czajkowski *et al.* and McMahan *et al.* embrace the soft modes heuristic by introducing elastic models whose stresses drive the kirigami's effective deformations towards cell-averaged local mechanisms. These models account for the geometric nonlinearity inherent to soft modes. However, they are based solely on deformations, and miss the fact that some sources of elastic frustration in kirigami arise instead from 'micro'-incompatibilities.

To illustrate this point, consider the 'domain wall' drawn in figure 2, which we base on an experiment in [28]. An initially open rotating-squares specimen (figure 2*a*) has two symmetry-related slit actuations that result in the same cell-averaged deformation, the 'red' and 'blue' phases in figure 2*b*,*c*. Forcing opposite phases to coexist leads to elastic frustration and to the appearance of a domain wall motif familiar from other materials applications [36–38]. This frustration is due to the microscale incompatibility of the two phases, which are nevertheless macroscopically compatible from the viewpoint of their effective deformations (both phases achieve the same overall shape change in figure 2*c*). Thus, domain walls cannot be captured with a model based only on cell-averaged deformations. The fix is to introduce an angle into the model that distinguishes between the two slit-actuations of the incompatible phases. In this way, Deng *et al.* predict a one-dimensional profile for the slit actuation across the wall, for sufficiently small displacements allowing the two-dimensional character of the wall to be neglected. We embrace the key insight of including the actuation, and incorporate it here into a nonlinear model.

Elastic continuum models with additional fields are known as *generalized elastic continua*. Such models were proposed by the Cosserat brothers in the late 1800s, and later codified in great detail in the works of Eringen (in [39] and references therein). Popular incarnations include micropolar and micromorphic elasticity; in general, a microcontinuum model uses auxilliary continuum fields to capture mechanical rearrangements at the microscale with consequences for elasticity at larger scales. For this reason, perhaps, recent research on metamaterials has made connections to this classical subject [40–42]. Nevertheless, the most familiar microcontinuum models do not appear to apply broadly to mechanical metamaterials, whose micro-motions are generally nonlinear. On a related note, there has been a systematic effort to coarse-grain the linear response of discrete truss structures including the Pantographic lattice [43–46], with the aim of setting strain-gradient and higher order effective continuum models on rigorous grounds. However, these results are limited to small displacements and linear elastic responses.

A key task in the continuum modelling of mechanism-based metamaterials is to link the (fundamentally nonlinear) micro-motions of the panels in a soft mode to the effective, macro-scale shape change. Our recent work [47] accomplishes this for planar kirigami with a nonlinear partial differential equation (PDE) relating the micro- and macro-scale motions. However, enforcing this PDE as a purely geometric constraint on the effective deformation neglects higher-order elastic effects present at the micro-scale, which contain information needed to formulate and solve elastic boundary value problems. We address this issue in this paper by positing a second-gradient like (actually mechanism gradient) generalized continuum model that enables us to solve for the response of the kirigami to general boundary conditions and loads.

Specifically, we present a generalized elastic continuum model for planar kirigami that accounts for the geometric nonlinearity of its soft modes. For concreteness and simplicity, we focus on a model system termed *rhombi-slit* krigami as it features periodic patterns of quad panels and rhombi slits. All such patterns possess a periodic mechanism fully parametrized by a quantity we call the *slit actuation*; all such patterns also exhibit locally mechanistic soft modes, whose effective description is captured by the PDE derived in [47]. Here, we build the PDE into a constitutive model with a bulk elastic energy that vanishes on its solutions, yielding an effective stress that vanishes on soft modes. The model also includes two higher-order sources of elasticity of physical origin [27,32], which we model using the slit actuation field: its gradient accounts for deviations from a pure mechanism, while its value accounts for hinge bending. Altogether, these three terms furnish a generalized elastic continuum model for rhombi-slit krigami in the plane. This new continuum constitutive model provides a versatile framework for solving elastic boundary value problems using a standard FEM platform (Abaqus). We demonstrate this versatility by comparing simulations to experiments across designs and loading conditions.

The rest of this paper is organized as follows. Section 2 describes the geometry of rhombi-slit kirigami and parametrizes their mechanisms. Section 3 introduces our generalized elastic continuum model. Section 4 derives its equilibrium equations and provides a finite-element formulation. Section 5 compares simulations of the model to experiments; the model reproduces heterogeneous displacement fields as well as a force–displacement curve. Section 6 ends with concluding remarks.

2. Kirigami patterns and their mechanisms

To introduce the design and kinematic variables of our model, we first treat the kirigami's simplest modes of deformation: its pure mechanisms.

(a) Rhombi-slit kirigami designs

We consider planar kirigami metamaterials consisting of a periodic array of unit cells, each having four quadrilateral panels and four rhombi-slits, as in figure 3*a*. In such designs, the four panels of the cell have identical shape and are mirrors of each other across the slit-axes. We use edge lengths a, b and c and two sector angles θ_{ab} and θ_{ac} to describe the shape of the quadrilateral panels. We also denote by ξ_0 the half opening angle of the central slit of the cell in its reference configuration. These six parameters are sketched in figure 3*a* and fully parameterize the unit cell, up to a rigid motion. This family of metamaterials has a large design space: it includes the well-known rotating-squares patterns ($a = b = c$, $\theta_{ab} = \theta_{ac} = \pi/2$) in its closed state ($\xi_0 = 0$) or open state ($\xi_0 = \pi/4$).

(b) Effective description of kirigami mechanisms

Each rhombi-slit kirigami possesses a single degree-of-freedom planar mechanism. We now recall the relevant results from [47], which link the kirigami's effective deformation to its slit actuation.

Let $\mathbf{e}_1$ and $\mathbf{e}_2$ denote the standard two-dimensional Cartesian basis. The vectors $\mathbf{s}_0$ and $\mathbf{t}_0$ in figure 3*a* are Bravais lattice vectors reflecting the periodicity of the pattern in its reference configuration. They can be written explicitly in terms of the cell parameters as

$$\begin{aligned} \mathbf{s}_0 &= 2(a\cos\xi_0 + b\cos(\pi - \theta_{ab} - \xi_0))\mathbf{e}_1, \\ \mathbf{t}_0 &= 2\left(a\sin\xi_0 + c\cos\left(\frac{\pi}{2} - \theta_{ac} + \xi_0\right)\right)\mathbf{e}_2. \end{aligned} \tag{2.1}$$

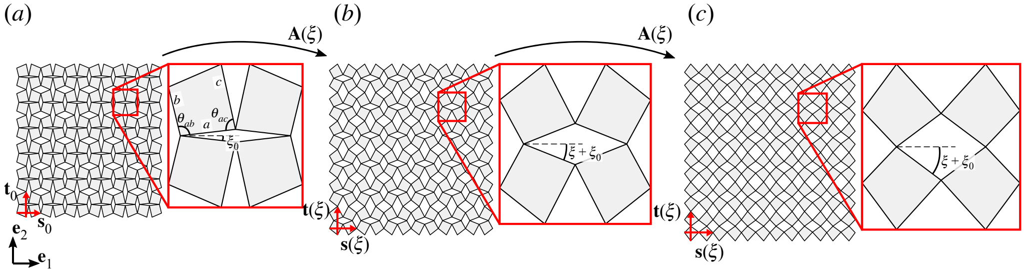

Figure 3. Effective deformation of a planar kirigami metamaterial made of periodic arrays of a unit cell featuring four quad panels and four rhombi-slits. (*a*) Reference configuration, with detail of a unit cell and its characteristic dimensions. Panels have side lengths a, b, c and internal angles θ_{ab} and θ_{ac}. The central slit has an initial opening angle $2\xi_0$. (*b*,*c*) Instances of the pure mechanism motion of the metamaterial in (*a*). During the mechanism motion, the unit cell represented by Bravais lattice vectors $\mathbf{s}_0$ and $\mathbf{t}_0$ in (*a*) is stretched and rotated, according to the stretch tensor $\mathbf{A}(\xi)$, where 2ξ is the change of opening angle of the central slit. Correspondingly, the lattice vectors deform to $\mathbf{s}(\xi)$ and $\mathbf{t}(\xi)$.

Now replace ξ_0 by $\xi_0 + \xi$ and observe from figure 3*b*,*c* that this change results in a deformed configuration of the pattern, where the central slit of each cell opens by an angle 2ξ and the panels counter-rotate to accommodate this actuation. In other words, slit actuation by ξ parametrizes a mechanism deformation of the pattern. As shown, the deformed configuration has the Bravais lattice vectors

$$\begin{aligned}\mathbf{s}(\xi) &= 2(a\cos(\xi_0+\xi) + b\cos(\pi-\theta_{ab}-\xi_0-\xi))\mathbf{e}_1,\\ \mathbf{t}(\xi) &= 2\left(a\sin(\xi_0+\xi) + c\cos\left(\frac{\pi}{2}-\theta_{ac}+\xi_0+\xi\right)\right)\mathbf{e}_2.\end{aligned} \tag{2.2}$$

To track the shape-change associated with this mechanism, we introduced a *shape tensor* $\mathbf{A}(\xi)$. This 2×2 tensor is defined as the unique linear transformation taking the reference Bravais lattice vectors to their deformed counterparts. It is determined as a function of the slit actuation ξ via

$$\mathbf{s}(\xi) = \mathbf{A}(\xi)\mathbf{s}_0 \quad \text{and} \quad \mathbf{t}(\xi) = \mathbf{A}(\xi)\mathbf{t}_0. \tag{2.3}$$

The explicit formula for $\mathbf{A}(\xi)$ in the case of rhombi-slit kirigami is

$$\begin{aligned}&\mathbf{A}(\xi) = (\cos\xi - \alpha\sin\xi)\mathbf{e}_1\otimes\mathbf{e}_1 + (\cos\xi + \beta\sin\xi)\mathbf{e}_2\otimes\mathbf{e}_2,\\ &\alpha = \frac{a\sin\xi_0 - b\sin(\theta_{ab}+\xi_0)}{a\cos\xi_0 - b\cos(\theta_{ab}+\xi_0)}, \qquad \beta = \frac{-c\cos(\theta_{ac}-\xi_0) + a\cos\xi_0}{c\sin(\theta_{ac}-\xi_0) + a\sin\xi_0}.\end{aligned} \tag{2.4}$$

Likewise, to coarse-grain the panel motions we introduced a two-dimensional *effective deformation* $\mathbf{y}_{\text{eff}}(\mathbf{x})$ per the Cauchy–Born rule. Since all cells deform identically in a mechanism, the associated $\mathbf{y}_{\text{eff}}(\mathbf{x})$ is homogeneous. Its 2×2 deformation gradient $\mathbf{F}_{\text{eff}}$ is constant, and is parametrized by the shape tensor up to a rigid rotation. We showed that

$$\text{(pure mechanism:)} \quad (\mathbf{F}_{\text{eff}})^{\mathrm{T}}\mathbf{F}_{\text{eff}} = \mathbf{A}^2(\xi) \tag{2.5}$$

thereby quantifying the link between the effective deformation of a mechanism and its slit actuation, ξ. By varying ξ, one obtains a compact description of the effective shape change.

Finding the shape tensor of a periodic mechanical metamaterial is a general way of linking its micro-scale motion to its macro-scale deformations, which we have just demonstrated for the pure mechanisms of rhombi-slit kirigami. The same approach applies to the more general family of parallelogram-slit kirigami, and goes beyond its mechanisms to capture its soft modes [47]. Certain generalized Miura–Ori origami patterns have been similarly coarse-grained in [33,35]. We focus on the class of rhombi-slit kirigami here because we think it strikes a balance between breadth and simplicity. Its simplicity is reflected in the fact that its shape tensor is diagonal (equation (2.4)), reflecting a locally bi-axial shape change. Its breadth will become clearer as we go on to describe a model for predicting the wealth of non-homogeneous soft modes.

3. A generalized continuum model for planar kirigami

We now present a constitutive model for the elasticity of rhombi-slit kirigami, based on the effective description of its mechanisms recalled in the previous section. As noted in the introduction, the basic experimental observation is that for a large class of loading conditions, the kirigami exhibits a soft response that cannot be captured by any single mechanism. Instead, its cells deform by an approximately locally mechanistic response, with an actuation that varies slowly from cell to cell, and with panel deformations that appear to oscillate about some smooth continuum deformation. We therefore build a generalized continuum model to predict the deformation and its underlying actuation.

(a) Statement of the model

For a rhombi-slit kirigami filling a two-dimensional reference domain Ω, let $\mathbf{y}_{\text{eff}} : \Omega \to \mathbb{R}^2$ denote its effective deformation and $\xi : \Omega \to \mathbb{R}$ its slit actuation, both of which we understand as continuum fields. Building off equation (2.5), our general idea is to choose an energy whose leading order behaviour prefers approximate local mechanisms. That is, we will require the model to produce the response

$$\text{(approx. locally mechanistic:)} \quad (\nabla \mathbf{y}_{\text{eff}}(\mathbf{x}))^{\mathrm{T}} \nabla \mathbf{y}_{\text{eff}}(\mathbf{x}) \approx \mathbf{A}^2(\xi(\mathbf{x})). \tag{3.1}$$

The pattern's slit actuation ξ will be treated as an auxiliary field variable governed by higher-order sources of elasticity in addition to this leading-order constraint.

Proceeding to details, we assume that the fields $(\mathbf{y}_{\text{eff}}, \xi)$ describing the kirigami's response to loads are (local) minimizers of the potential energy function

$$\begin{gathered}\mathcal{E}(\mathbf{y}_{\text{eff}}, \xi) = \int_{\Omega} W(\nabla \mathbf{y}_{\text{eff}}(\mathbf{x}), \xi(\mathbf{x}), \nabla \xi(\mathbf{x}))\, \mathrm{d}A - \int_{\partial_t \Omega} \mathbf{t}_R(\mathbf{x}) \cdot \mathbf{y}(\mathbf{x})\, \mathrm{d}\Gamma \\ \text{subject to } \mathbf{y}_{\text{eff}}(\mathbf{x}) = \mathbf{y}_{\text{b}}(\mathbf{x}) \text{ on } \partial\Omega \setminus \partial_t \Omega,\end{gathered} \tag{3.2}$$

where $\mathbf{t}_R$ denotes a prescribed 'reference' traction on the boundary component $\partial_t \Omega \subset \partial \Omega$, and $\mathbf{y}_{\text{b}}$ prescribes the deformation on the rest of the boundary. We use the strain energy density

$$W(\mathbf{F}, \theta, \mathbf{p}) = c_0 W_0(\mathbf{F}\mathbf{A}^{-1}(\theta)) + c_1 \theta^2 + c_2 |\mathbf{p}|^2. \tag{3.3}$$

Its first term, W_0, takes the form of a standard isotropic two-dimensional hyperelastic model

$$W_0(\mathbf{G}) = \left(\frac{1}{J_{\mathbf{G}}} |\mathbf{G}|^2 - 2 \right) + (J_{\mathbf{G}} - 1)^2 \tag{3.4}$$

up to the decomposition $\mathbf{G} = \mathbf{F}\mathbf{A}^{-1}(\theta)$. Here $\mathbf{A}(\theta)$ is the shape tensor, encoding the geometry of the reference pattern from §2a; it is invertible for any physical value of slit actuation. Note $J_{\mathbf{G}} = \det \mathbf{G}$ for short. Finally, the parameters c_0, c_1, c_2 are elastic moduli which we anticipate fitting to experiments.

(b) Physical origin of the model

Using figure 4 as a guide, we now discuss the physical origin of the three terms in the energy density. Each term is a distinct and natural consequence of the disparity of lengthscales in the pattern. As sketched in figure 4*a*,*c*–*f*, L is the sample lengthscale, ℓ the unit cell lengthscale, and δ the hinge lengthscale. Though our model can be generally applied, it is most relevant when $\delta \ll \ell \ll L$, i.e. when the number of unit cells in the sample is large, and the hinges are small as compared to the panels. We make this assumption throughout.

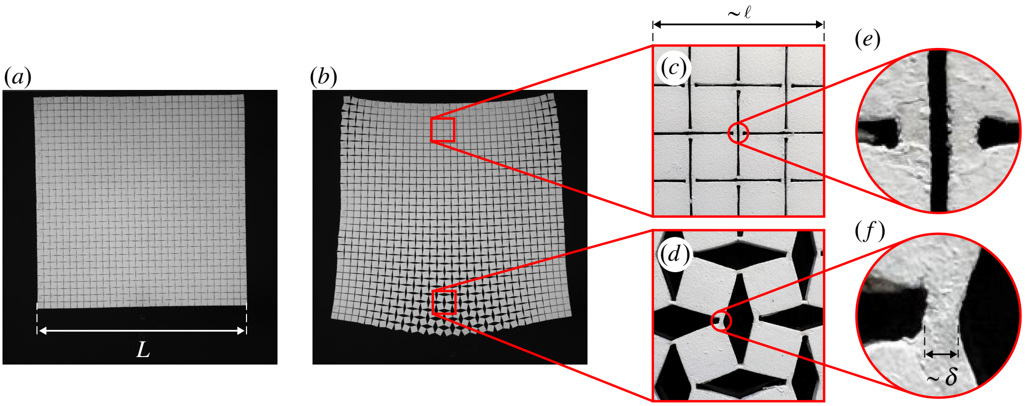

Figure 4. Illustration of the characteristic lengthscales of a rhombi-slit kirigami metamaterial. (*a*) Reference, undeformed configuration, indicating the sample lengthscale L. (*b*) Same pattern, subjected to heterogeneous loading. (*c*,*d*) Zoom-in on slightly deformed and significantly deformed regions of the specimen, through a window of dimensions comparable to the unit cell lengthscale ℓ. (*e*,*f*) Zoom-in on the hinges, indicating the hinge lengthscale δ.

The first term in equation (3.3), W_0, arises as follows. Suppose we focus solely on regions of length $\sim\ell$ under typical loading, like those in figure 4*c*,*d*. The local response is then nearly indistinguishable from that of a pure mechanism; the heterogeneity, as seen in figure 4*b*, only emerges at a much larger scale. Because of this feature, we choose W_0 to be a bulk elastic energy that is minimized and zero whenever $(\mathbf{y}_{\text{eff}}, \xi)$ coincides with a coarse-grained local mechanism,

$$\text{(locally mechanistic:)} \quad (\nabla\mathbf{y}_{\text{eff}}(\mathbf{x}))^{\mathrm{T}}\nabla\mathbf{y}_{\text{eff}}(\mathbf{x}) = \mathbf{A}^2(\xi(\mathbf{x})). \tag{3.5}$$

Choosing W_0 as such introduces stress proportional to the modulus c_0 to penalize deviations from local mechanisms. This stress should be significant. In fact, as was described in the electronic supplementary material of our previous work [47], a coarse-grained kirigami deformation that fails to be locally mechanistic is accompanied by distortions of the panels and hinges comparable to the characteristic length of the panels ($\sim\ell$). As such, c_0 should scale with the shear modulus μ of the material used to fabricate the kirigami (possibly with some weak dependence on ℓ/L or δ/ℓ).

The other two terms in the energy density equation (3.3) account for higher order effects related to localized elastic distortions in and nearby the hinges. The second term (with modulus c_1) is the simplest possible model that approximates the bending energy of the hinges when slits open or close. In the effective description, it depends only on the slit actuation angle ξ. This actuation counter-rotates the panels to yield the bending, as shown in figure 4*d*,*f*. Large actuation causes localized strains $\sim|\xi|$ nearby the hinges, which give a bending energy per cell $\sim\mu|\xi|^2\delta^2$ since the hinges occupy an area $\sim\delta^2$. As the cell area is $\sim\ell^2$, the corresponding modulus c_1 in equation (3.3) scales as $c_1 \sim \mu\delta^2/\ell^2$.

The final term in the energy density equation (3.3) regularizes the actuation field, and corresponds to the simplest elastic model for resisting inhomogeneous actuation in a locally mechanistic response (i.e. 'mechanism gradients'). This term is akin to the strain-gradient term in [32] and the plate bending term from McMahan *et al.* [34], which, respectively, regularize mechanism gradients via second gradients of the effective in- and out-of-plane displacements. By contrast, our model depends directly on the actuation gradient $\nabla\xi$. As such, it accounts for all possible micro-incompatibilities, including those that lead to a homogeneous effective displacement, and that would be spuriously assigned no strain-gradient/plate bending energy. Figure 2 from the introduction gives an example.

Our mechanism gradient term also has physical origins [27]. Where the kirigami's response deviates from a single mechanism, elastic distortions are required to preserve the connectivity of the pattern. For a locally mechanistic deformation with a smoothly varying actuation field ξ, one expects the required distortions to be $\sim\ell^2|\nabla\xi|$ in magnitude, and to be accompanied by panel strains $\sim\ell|\nabla\xi|$ [47]. (In fact, there is a subtle logarithmic correction to these scalings involving a self-similar spreading of strains which will be the topic of forthcoming work [48].) This argument gives an energy per cell $\sim\mu\ell^2|\nabla\xi|^2\ell^2$ since each cell has area $\sim\ell^2$. The corresponding modulus c_2 in equation (3.3) scales as $c_2 \sim \mu\ell^2$. Postponing the detailed derivation of the fully tensorial mechanism gradient term to future work [48], we simply choose to model it here using a straightforward constitutive model that contains all the necessary sources of elasticity.

(c) Effective stress and effectively stress-free configurations

Having written down an effective model, we proceed to determine the effective stress measures it imposes, and derive and discuss some properties of effectively stress-free configurations. The first Piola–Kirichhoff stress **P** is obtained by differentiating the strain energy density W in **F**. From equation (3.3),

$$\mathbf{P}(\mathbf{F},\theta) = \mathbf{P}_0(\mathbf{F}\mathbf{A}^{-1}(\theta))\mathbf{A}^{-T}(\theta) \tag{3.6}$$

for the two-dimensional hyperelastic first Piola–Kirchhoff stress

$$\mathbf{P}_0(\mathbf{G}) := c_0\frac{\partial W_0(\mathbf{G})}{\partial \mathbf{G}} = \frac{c_0}{J_{\mathbf{G}}}(2\mathbf{G} + (2(J_{\mathbf{G}}^3 - J_{\mathbf{G}}^2) - |\mathbf{G}|^2)\mathbf{G}^{-T}). \tag{3.7}$$

We also introduce the so-called Kirchhoff stress [49], as it will be useful later on for numerics. This stress is defined as

$$\boldsymbol{\tau}(\mathbf{F},\theta) := \mathbf{P}(\mathbf{F},\theta)\mathbf{F}^{\mathrm{T}} = \mathbf{P}_0(\mathbf{F}\mathbf{A}^{-1}(\theta))(\mathbf{F}\mathbf{A}^{-1}(\theta))^{\mathrm{T}} = \boldsymbol{\tau}_0(\mathbf{F}\mathbf{A}^{-1}(\theta)) \tag{3.8}$$

for the two-dimensional hyperelastic Kirchhoff stress

$$\boldsymbol{\tau}_0(\mathbf{G}) := \mathbf{P}_0(\mathbf{G})\mathbf{G}^{\mathrm{T}} = \frac{c_0}{J_{\mathbf{G}}}(2\mathbf{G}\mathbf{G}^{\mathrm{T}} + (2(J_{\mathbf{G}}^3 - J_{\mathbf{G}}^2) - |\mathbf{G}|^2)\mathbf{I}). \tag{3.9}$$

In a traditional elastic continuum, the stress-free configurations are rigid body motions. Indeed, $\boldsymbol{\tau}_0(\mathbf{G}) = \mathbf{0}$ if and only if **G** is a rotation. By contrast, our generalized continuum model has a much richer family of effectively stress-free configurations: for the fields $(\mathbf{y}_{\mathrm{eff}}, \xi)$ on Ω,

$$\boldsymbol{\tau}(\nabla\mathbf{y}_{\mathrm{eff}}(\mathbf{x}), \xi(\mathbf{x})) = \mathbf{0} \quad \Leftrightarrow \quad (\nabla\mathbf{y}_{\mathrm{eff}}(\mathbf{x}))^{\mathrm{T}}\nabla\mathbf{y}_{\mathrm{eff}}(\mathbf{x}) = \mathbf{A}^2(\xi(\mathbf{x})). \tag{3.10}$$

The latter equation is the condition for a coarse-grained local mechanism discussed above (equation (3.5)). It constrains the metric tensor (right Cauchy–Green tensor) of the effective deformation $\mathbf{y}_{\mathrm{eff}}$ in terms of the slit actuation field ξ, which reflects the fact that the effective fields must vary in a coordinated way to represent a locally mechanistic soft mode of rhombi-slit kirigami in the plane.

In our previous work [47], we showed that there are broad classes of deformations and slit actuations that solve this metric constraint, and that these fields capture the behaviour of soft deformations observed experimentally. We also derived an important link between the metric constraint and the effective Poisson's ratio of the pattern. We present a brief description of this link here, as it illuminates a fundamental dichotomy in the qualitative features of the slit actuation in this model, and will help to clarify the choices we make later on in the simulations and experiments.

Consider any effectively stress-free configuration $(\mathbf{y}_{\mathrm{eff}}, \xi)$, i.e. one with $\boldsymbol{\tau} = \mathbf{0}$. Since the deformation is planar, it trivially has zero Gauss curvature. As the Gauss curvature is fundamentally linked to its metric tensor through Gauss's remarkable theorem [50], we find that the slit actuation solves a PDE of the form

$$\left[\partial_2^2 - \left(\frac{\mu_1(\xi(\mathbf{x}))}{\mu_2(\xi(\mathbf{x}))}\right)^2 \nu_{21}(\xi(\mathbf{x}))\partial_1^2\right]\xi(\mathbf{x}) = g(\xi(\mathbf{x}), \nabla\xi(\mathbf{x})), \tag{3.11}$$

for $g(\theta, \mathbf{p})$ a function whose explicit form is lengthy and not important for the discussion at hand. The function $\nu_{21}(\theta)$, introduced in this PDE, turns out to be the effective Possion's ratio of the pattern. It satisfies

$$\nu_{21}(\theta) = \frac{(\cos\theta - \alpha\sin\theta)}{(\sin\theta + \alpha\cos\theta)}\frac{(-\sin\theta + \beta\cos\theta)}{(\cos\theta + \beta\sin\theta)} \tag{3.12}$$

where α and β quantify the reference rhombi-slit cell via equation (2.4).

The PDE in equation (3.11) is second order and quasi-linear, which means that its so-called *type* has a standard classification from PDE theory [51]: the PDE is elliptic for solutions ξ that satisfy $\nu_{21}(\xi(\mathbf{x})) < 0$ on Ω, is hyperbolic for solutions that satisfy $\nu_{21}(\xi(\mathbf{x})) > 0$ on Ω, and is of mixed type if the solution's Poisson's ratio changes sign on some part of the domain. In other words, the PDE is elliptic if the unit cell is auxetic and hyperbolic if it is *non*-auxetic.

These results have important modelling implications. In the typical setting, where $c_0 \gg c_{1,2}$ in equation (3.3), we expect a large family of 'slightly stressed' equilibrium solutions of our model. Each such solution, then, approximately solves the metric constraint, with a ξ field that closely resembles one obeying the PDE in equation (3.11). Given this observation, we identify rhombi-slit kirigami as elliptic or hyperbolic based on the sign of its effective Poisson's ratio at equilibrium. We expect this identification to indicate certain qualitative properties of the kirigami's response to loads: elliptic kirigami with auxetic cells should exhibit a decay in slit actuation away from the boundary loads. By contrast, hyperbolic kirigami with non-auxetic cells should exhibit comparatively persistent slit actuation under the same loading conditions. We highlight this dichotomy in further detail with the examples to come.

4. Equilibrium equations and finite-element formulation

Next, we derive the equilibrium equations and natural boundary conditions of our model. The equilibrium equations are a coupled PDE system that includes the familiar divergence-free condition on the effective stress, as well as an auxiliary PDE enforcing equilibrium for the slit actuation. We finish this section with an FEM formulation of the model, and discuss its implementation in Abaqus.

(a) Derivation of equilibrium equations

We first derive the equilibrium equations. Let $(\mathbf{y}_{\text{eff}}, \xi)$ be a local minimizer to the potential energy in equation (3.2). Then, by taking the first variation of the energy functional,

$$\begin{aligned} 0 &= \frac{\mathrm{d}}{\mathrm{d}\epsilon}\mathcal{E}(\mathbf{y}_{\text{eff}} + \epsilon\mathbf{w}, \xi + \epsilon\eta)\big|_{\epsilon=0} \\ &= \int_\Omega \mathbf{P}(\nabla\mathbf{y}_{\text{eff}}(\mathbf{x}), \xi(\mathbf{x})) : \nabla\mathbf{w}(\mathbf{x})\,\mathrm{d}A - \int_{\partial_t\Omega} \mathbf{t}_R(\mathbf{x})\cdot\mathbf{w}(\mathbf{x})\,\mathrm{d}\Gamma \\ &\quad + \int_\Omega \{W_\theta(\nabla\mathbf{y}_{\text{eff}}(\mathbf{x}), \xi(\mathbf{x}), \nabla\xi(\mathbf{x}))\eta(\mathbf{x}) + W_{\mathbf{p}}(\nabla\mathbf{y}_{\text{eff}}(\mathbf{x}), \xi(\mathbf{x}), \nabla\xi(\mathbf{x}))\cdot\nabla\eta(\mathbf{x})\}\,\mathrm{d}A \end{aligned} \tag{4.1}$$

for all sufficiently smooth $\mathbf{w} : \Omega \to \mathbb{R}^2$ satisfying $\mathbf{w}(\mathbf{x}) = \mathbf{0}$ on $\partial\Omega \setminus \partial_t\Omega$, and $\eta : \Omega \to \mathbb{R}$. Here and throughout, we use a colon to denote the contraction of square matrices $\mathbf{S} : \mathbf{T} = \mathrm{Tr}(\mathbf{S}^{\mathrm{T}}\mathbf{T})$. In addition, W_θ and $W_{\mathbf{p}}$ denote the partial derivatives of $W(\mathbf{F}, \theta, \mathbf{p})$ with respect to θ and $\mathbf{p}$. Observe that

$$\begin{aligned} W_\theta(\mathbf{F},\theta,\mathbf{p}) &= \underbrace{-\mathbf{P}_0(\mathbf{F}\mathbf{A}^{-1}(\theta)) : (\mathbf{F}\mathbf{A}^{-1}(\theta)\mathbf{A}'(\theta)\mathbf{A}^{-1}(\theta)) + 2c_1\theta}_{=:f_{\mathrm{act}}(\mathbf{F},\theta)}, \\ W_{\mathbf{p}}(\mathbf{F},\theta,\mathbf{p}) &= 2c_2\mathbf{p}. \end{aligned} \tag{4.2}$$

We show below that $f_{\mathrm{act}}(\mathbf{F},\theta)$ provides a driving force for heterogeneous actuation within the model.

We substitute these formulae into equation (4.1), let $\mathbf{P}_{\mathbf{y}_{\mathrm{eff}},\xi}(\mathbf{x}) := \mathbf{P}(\nabla\mathbf{y}_{\mathrm{eff}}(\mathbf{x}), \xi(\mathbf{x}))$ and apply the divergence theorem with the usual localization arguments to conclude the following equilibrium equations on Ω:

$$\begin{aligned} \nabla \cdot (\mathbf{P}^{\mathrm{T}}_{\mathbf{y}_{\mathrm{eff}},\xi}(\mathbf{x})) &= \mathbf{0}, \\ f_{\mathrm{act}}(\nabla\mathbf{y}_{\mathrm{eff}}(\mathbf{x}), \xi(\mathbf{x})) &= 2c_2\nabla^2\xi(\mathbf{x}). \end{aligned} \tag{4.3}$$

The terminology for f_{act} can now be understood, since the actuation at equilibrium is heterogeneous ($\nabla\xi \neq 0$) whenever f_{act} is non-zero. Likewise, we derive the boundary conditions

$$\begin{cases} \mathbf{P}_{\mathbf{y}_{\mathrm{eff}},\xi}(\mathbf{x})\mathbf{n}_R(\mathbf{x}) = \mathbf{t}_R(\mathbf{x}) & \text{on } \partial_t\Omega \\ \mathbf{y}_{\mathrm{eff}}(\mathbf{x}) = \mathbf{y}_{\mathrm{b}}(\mathbf{x}) & \text{on } \partial\Omega \setminus \partial_t\Omega \\ \nabla\xi(\mathbf{x}) \cdot \mathbf{n}_R(\mathbf{x}) = 0 & \text{on } \partial\Omega \end{cases} \tag{4.4}$$

where $\mathbf{n}_R(\mathbf{x})$ denotes the outwards-pointing unit normal at a point $\mathbf{x}$ on the boundary of Ω.

(b) Finite-element formulation

To solve these equations, we use the finite-element method (FEM). Equations (4.3) and (4.4) give the strong form of the boundary value problem for the effective deformation $\mathbf{y}_{\mathrm{eff}}$ and slit actuation field ξ. FEM formulations are instead based on the weak form, in equation (4.1). Using equation (4.2), we can conveniently rewrite the weak form as

$$\begin{aligned} \int_\Omega \mathbf{P}(\nabla\mathbf{y}_{\mathrm{eff}}(\mathbf{x}), \xi(\mathbf{x})) : \nabla\mathbf{w}(\mathbf{x})\,\mathrm{d}A - \int_{\partial_t\Omega} \mathbf{t}_R(\mathbf{x}) \cdot \mathbf{w}(\mathbf{x})\,\mathrm{d}\Gamma &= \mathbf{0}, \\ \int_\Omega \{f_{\mathrm{act}}(\nabla\mathbf{y}_{\mathrm{eff}}(\mathbf{x}), \xi(\mathbf{x}))\eta(\mathbf{x}) + 2c_2\nabla\xi(\mathbf{x}) \cdot \nabla\eta(\mathbf{x})\}\,\mathrm{d}A &= 0 \end{aligned} \tag{4.5}$$

for all sufficiently smooth $\mathbf{w}(\mathbf{x})$ with $\mathbf{w}(\mathbf{x}) = \mathbf{0}$ on $\partial\Omega \setminus \partial_t\Omega$ and all $\eta(\mathbf{x})$.

To numerically approximate a solution of equation (4.5), we mesh Ω and set

$$\begin{aligned} \mathbf{y}_{\mathrm{eff}}(\mathbf{x}) = \mathbf{x} + \sum_A \mathbf{u}^A N^A(\mathbf{x}), \quad \mathbf{w}(\mathbf{x}) = \sum_A \mathbf{w}^A N^A(\mathbf{x}), \\ \xi(\mathbf{x}) = \sum_A \xi^A N^A(\mathbf{x}), \quad \eta(\mathbf{x}) = \sum_A \eta^A N^A(\mathbf{x}). \end{aligned} \tag{4.6}$$

The quantities $\mathbf{u}^A, \mathbf{w}^A \in \mathbb{R}^2$, and $\xi^A, \eta^A \in \mathbb{R}$ denote the nodal values of the respective fields at the mesh points $\mathbf{x}^A \in \Omega$, indexed by A; $N^A(\mathbf{x})$ is the corresponding shape function with standard properties. For organizational purposes, we list all the nodal values $\mathbf{u}^A$ and ξ^A as arrays $\mathbf{u}$ and $\boldsymbol{\xi}$.

We substitute equation (4.6) into equation (4.5) and use that each η^A is arbitrary and each $\mathbf{w}^A$ is arbitrary for $\mathbf{x}^A \notin \partial\Omega \setminus \partial_t\Omega$. After some standard manipulations, we conclude that $\mathbf{u}$ and $\boldsymbol{\xi}$ should ideally satisfy

$$\begin{aligned} \mathbf{r}^A_{\mathrm{force}}(\mathbf{u}, \boldsymbol{\xi}) = \mathbf{0} \quad & \text{for all } A \text{ such that } \mathbf{x}^A \notin \partial\Omega \setminus \partial_t\Omega, \\ r^A_{\mathrm{act}}(\mathbf{u}, \boldsymbol{\xi}) = 0 \quad & \text{for all } A. \end{aligned} \tag{4.7}$$

The residual force and actuation are given by

$$\begin{aligned}\mathbf{r}^A_{\text{force}}(\mathbf{u},\boldsymbol{\xi}) &= -\int_\Omega \mathbf{P}(\tilde{\mathbf{F}}(\mathbf{x},\mathbf{u}),\tilde{\theta}(\mathbf{x},\boldsymbol{\xi}))\nabla N^A(\mathbf{x})\,\mathrm{d}A + \int_{\partial_t\Omega} \mathbf{t}_R(\mathbf{x})N^A(\mathbf{x})\,\mathrm{d}\Gamma,\\ r^A_{\text{act}}(\mathbf{u},\boldsymbol{\xi}) &= -\int_\Omega \{f_{\text{act}}(\tilde{\mathbf{F}}(\mathbf{x},\mathbf{u}),\tilde{\theta}(\mathbf{x},\boldsymbol{\xi}))N^A(\mathbf{x}) + 2c_2\tilde{\mathbf{p}}(\mathbf{x},\boldsymbol{\xi})\cdot\nabla N^A(\mathbf{x})\}\,\mathrm{d}A\end{aligned} \tag{4.8}$$

and the arguments for $\mathbf{P}(\cdot), f_{\text{act}}(\cdot)$, and so on in these formulae are defined as

$$\begin{aligned}&\tilde{\mathbf{F}}(\mathbf{x},\mathbf{u}) := \mathbf{I} + \sum_B \mathbf{u}^B\otimes\nabla N^B(\mathbf{x}),\quad \tilde{\theta}(\mathbf{x},\boldsymbol{\xi}) := \sum_B \xi^B N^B(\mathbf{x}),\\ &\tilde{\mathbf{p}}(\mathbf{x},\boldsymbol{\xi}) := \sum_B \xi^B \nabla N^B(\mathbf{x}).\end{aligned} \tag{4.9}$$

In practice, we do not solve for the arrays $(\mathbf{u},\boldsymbol{\xi})$ by making the residuals vanish. Instead, a Newton–Raphson scheme is employed in the FEM solver, which chooses nodal quantities by iterative linearization in an effort to make the residuals sufficiently small. The solver in Abaqus takes as input explicit functions of the derivatives of the residuals, i.e. the tangents

$$\begin{aligned}&\mathbf{K}^{AB}_{\text{disp}}(\mathbf{u},\boldsymbol{\xi}) := -\frac{\partial\mathbf{r}^A_{\text{force}}(\mathbf{u},\boldsymbol{\xi})}{\partial\mathbf{u}^B},\quad \mathbf{k}^{AB}_{\text{disp}}(\mathbf{u},\boldsymbol{\xi}) := -\frac{\partial r^A_{\text{act}}(\mathbf{u},\boldsymbol{\xi})}{\partial\mathbf{u}^B},\\ &k^{AB}_{\text{act}}(\mathbf{u},\boldsymbol{\xi}) := -\frac{\partial r^A_{\text{act}}(\mathbf{u},\boldsymbol{\xi})}{\partial\xi^B},\quad \mathbf{k}^{AB}_{\text{act}}(\mathbf{u},\boldsymbol{\xi}) := -\frac{\partial\mathbf{r}^A_{\text{force}}(\mathbf{u},\boldsymbol{\xi})}{\partial\xi^B}.\end{aligned} \tag{4.10}$$

Explicit formulae for these tangents are in appendix A.

Equation (4.8) and the formulae for equation (4.10) are integrals calculated numerically using Gaussian quadrature. The formulae for the shape functions, Gaussian quadrature, and the surface traction term are all standard, and not discussed here. We implement this FEM formulation into Abaqus using a user-element subroutine (UEL) [52]. The UEL is called for each element for each iteration. The initial nodal coordinates and current nodal variables $(\mathbf{u},\boldsymbol{\xi})$ are input. The nodal residuals in equation (4.8) and tangents in equation (4.10) are output. The UEL can be used for linear/quadratic and triangular/quadrilateral elements.

5. Experiments and simulations

To validate our model, we compare its predictions with experiments for two designs, namely, the auxetic rotating-squares sample and another that is strictly non-auxetic and is described just below. We define the geometry of the samples, including hinge regions, and explain how to extract a representative rhombi-slit cell for each design to facilitate a reasonable comparison between model and experiment. We study the simple example of uniform stretch, and then turn to complex examples involving heterogeneous loads.

(a) Experimental samples and their idealized unit cells

Figure 5*a*,*b* shows the two specimens used in our work. One is a classical rotating-squares pattern. The other—which we term as a ‘hyperbolic pattern’ for reasons explained below—features two alternating slits with the same width in the horizontal direction and different height. Figure 5*c*,*d* shows portions of the patterns that were used for laser cutting; the fabricated samples include hinge regions designed to be of length $d = \ell/20$ and height $h = \ell/80$, as shown. The actual hinge dimensions vary from the designed ones due to variability associated with laser cutting rubber.

To convert the two cut pattern designs into idealized rhombi-slit designs, we treat the centroid of each hinge as a corner point. Tracing out the lines connecting neighbouring corner points leads to a desired rhombi-slit pattern. We use these ‘traced’ rhombi-slit cells as inputs to the simulations. The parameters for both patterns are displayed in figure 5. Recalling equation (2.4), the rotating-squares pattern satisfies $(\alpha,\beta) = (-0.9, 0.9)$, while the hyperbolic pattern satisfies $(\alpha,\beta) = (-0.9, 0)$.

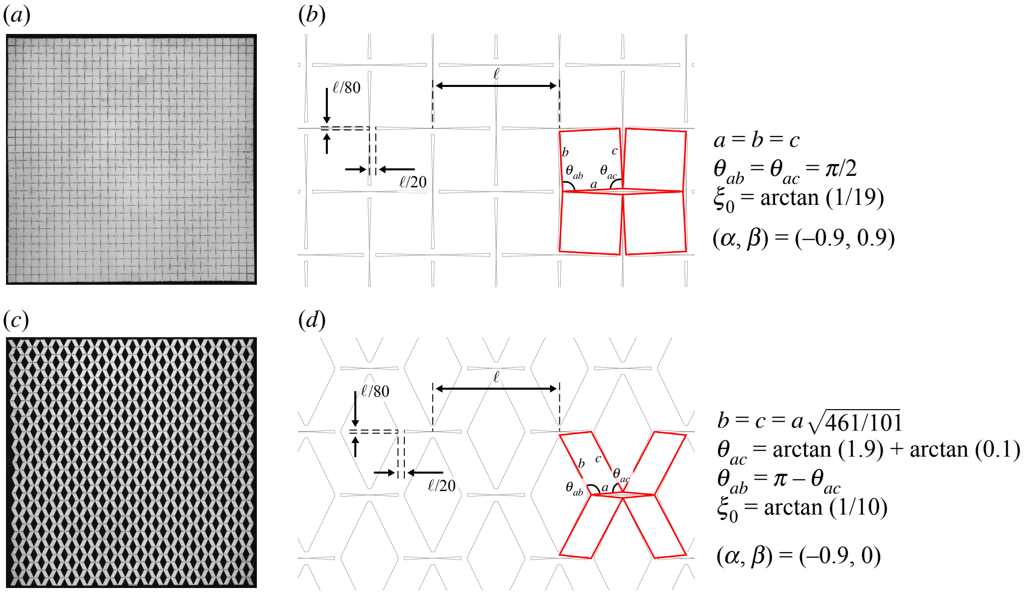

Figure 5. From fabricated patterns to idealized rhombi-slit cells. (*a*) Rotating-squares sample (elliptic). (*b*) Non-auxetic sample (hyperbolic). (*c*,*d*) Portions of the patterns fed to the laser cutter to fabricate specimens (*a*,*b*). To avoid issues during cutting, hinges are shaped as rectangular blocks. We highlight idealized unit cells in red and report their dimensions.

Substituting these parameters into equation (3.12) for the cell's effective Poisson's ratio gives

$$\begin{aligned} &\text{(Rotating-Squares:)} \quad \nu_{21}(\xi) = -1, \\ &\text{(Hyperbolic Pattern:)} \quad \nu_{21}(\xi) = \left(\frac{-\cos\xi + 0.9\sin\xi}{-0.9\cos\xi + \sin\xi}\right)\tan\xi \overset{|\xi|\ll 1}{\approx} 1.11\xi. \end{aligned} \tag{5.1}$$

As discussed in §3c, Poisson's ratio describes important qualitative features of each pattern's response, in addition to its auxeticity.

The rotating-squares pattern is auxetic and, more specifically, purely dilational, since Poisson's ratio indicates equal principal strains independent of the slit actuation. It therefore belongs to the special class of patterns known as *conformal* [32,47], which is a subclass of the more general elliptic kirigami discussed previously. We expect this pattern's actuation to generally decay away from boundary loads. By contrast, the hyperbolic pattern is non-auxetic, thus *hyperbolic*, for $\xi \in (0, 0.23\pi)$. The sample is termed hyperbolic because the slit actuation is always observed to be in the hyperbolic range for tension type boundary conditions. (By contrast, compressing the sample can lead to buckling, which we do not discuss here; see [34] for ideas in this direction.) Guided by its hyperbolicity, we expect this pattern's actuation to persist far away from boundary loads.

(b) Uniform stretch

The simple loading condition of uniform stretch allows us to investigate the interplay between hinge elasticity and the purely mechanistic response, both experimentally and in the elastic energy in equation (3.3). For the demonstration, we focus on the auxetic rotating-squares example. Experimentally, similarly to what is done in [53], we induce free transverse expansion under uniaxial loading by connecting the boundary slits on the left and right edges of the specimen to a rod by means of hooks, as illustrated in figure 6*a*. This connection allows transverse motion at little resistance. The experimental results, comparing stretch to slit actuation, are marked with circles in figure 6*b*.

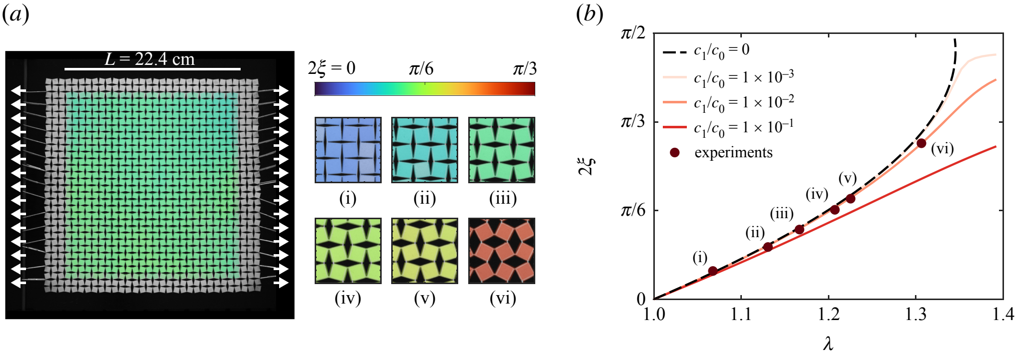

Figure 6. Uniform stretch of the rotating-squares sample. (*a*) Colour maps of the slit actuation, determined by the method described in appendix B. *L* is the undeformed sample length. (*b*) Slit actuation ξ plotted as a function of horizontal stretch λ. Solid lines display the model results with varying c_1/c_0.

The experimental pattern displays a mostly uniform actuation under this loading, especially in the centre of the sample as indicated. We therefore consider the elastic energy of the $(\alpha,\beta)=(-0.9,0.9)$ rotating-squares pattern under a homogeneous effective deformation gradient $\nabla\mathbf{y}_{\text{eff}}(\mathbf{x})=\mathbf{F}(\lambda,\lambda_2)=\lambda\mathbf{e}_1\otimes\mathbf{e}_1+\lambda_2\mathbf{e}_2\otimes\mathbf{e}_2$ and slit actuation $\xi(\mathbf{x})=\xi$. For a given stretch λ, equilibrium is achieved by minimizing $W(\mathbf{F}(\lambda,\lambda_2),\xi,\mathbf{0})$ with respect to λ_2 and ξ. Setting $w(\lambda,\xi):=\min_{\lambda_2}W(\mathbf{F}(\lambda,\lambda_2),\xi,\mathbf{0})$, the slit actuation at equilibrium is

$$\xi(\lambda)=\arg\min_{\xi}\{w(\lambda,\xi)\}. \tag{5.2}$$

The actuation depends implicitly on the ratio c_1/c_0, reflecting the relative influence of bulk and hinge elasticity in the model.

In figure 6*b*, we plot $(\lambda,2\xi(\lambda))$ for $c_1/c_0=0,10^{-1},10^{-2}$ and 10^{-3}. The bulk elastic term dominates at small values of stretch, since the plot is essentially independent of c_1/c_0 in this regime. As the stretch increases, hinge elasticity becomes more pronounced; the curve shows a particularly strong dependence on c_1/c_0 in the large stretch regime ($\lambda>1.2$). We note, generally, that the slit actuation decreases monotonically as a function of increasing c_1/c_0, and hinge elasticity cannot be ignored at large values of stretch for this sample. Also, the ratio $c_1/c_0=10^{-2}$ provides a good fit to our experimental data. We use $c_1/c_0=10^{-2}$ from here on when comparing the deformed rotating-squares sample to analogous simulations.

(c) Heterogeneous loading

We turn now to a comparison between FEM simulations of the model and experiments under complex loading conditions. We perform the FEM simulations in Abaqus/Standard using the UEL subroutine developed in §4b: a two-dimensional square domain non-dimensionalized to have unit length is meshed by 1600 (8 node quadratic quadrilateral) user elements and is subjected to various displacement boundary conditions. The model has three moduli c_0, c_1, c_2 which need to be supplied for the two samples, along with the cell parameters α and β from figure 5. We normalize the elasticity by c_0; this choice influences the overall magnitude of the stresses, but not the predicted deformation. As a side note, the need to fit c_0 will present itself in §5d. Lastly, we fit the ratios c_1/c_0 and c_2/c_0 so as to accurately capture the response of a broad range of experiments. For simplicity, the fit is done by trial and error for a variety of boundary conditions. Each simulation typically takes less than minute on a standard laptop, so this approach is not

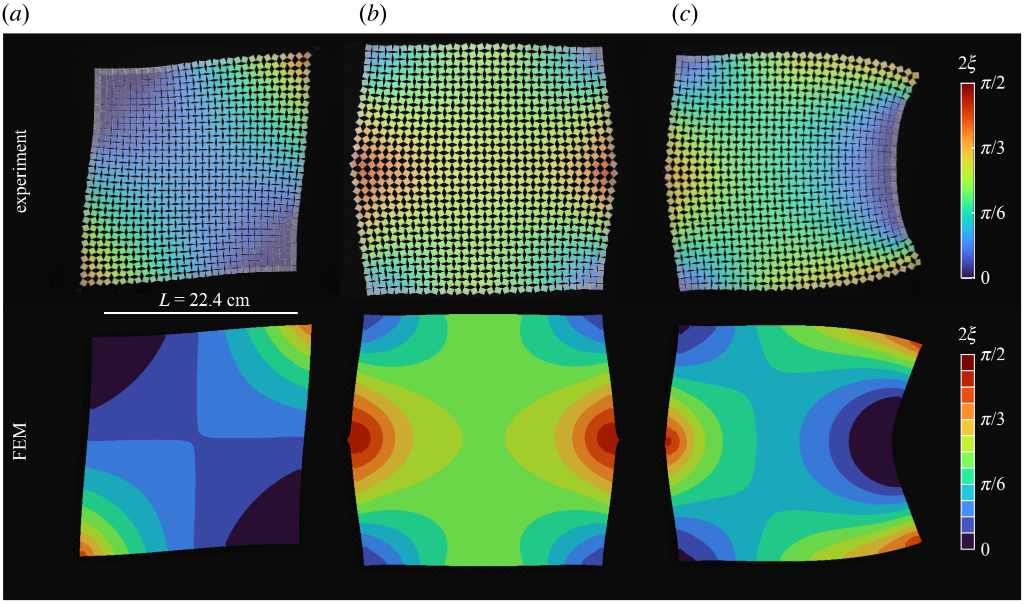

Figure 7. Experiments and simulations of rotating-squares sample. Three boundary conditions are applied: (*a*) pulling along diagonal line; (*b*) pulling along centreline; (*c*) pulling a centre point with opposite corner points fixed. L is the undeformed sample length. Colour maps show the slit actuation angle ξ, extracted from the experiment per appendix B.

tedious or difficult. In the following comparison, we use

$$\begin{aligned}
&\text{(Rotating-Squares:)} \quad \frac{c_1}{c_0} = 10^{-2}, \quad \frac{c_2}{c_0} = 5\times 10^{-5},\\
&\text{(Hyperbolic Pattern:)} \quad \frac{c_1}{c_0} = 3\times 10^{-2}, \quad \frac{c_2}{c_0} = 10^{-4}.
\end{aligned} \tag{5.3}$$

One should not extrapolate these values to other samples. We expect c_1/c_0 and c_2/c_0 to vary for patterns fabricated with a different number of cells or hinge-panel dimensions, even if the unit cell geometry and underlying material are otherwise the same. As discussed in §3a, basic physical reasoning suggests the scalings $c_1/c_0 \sim \delta^2/\ell^2$ and $c_2/c_0 \sim \ell^2$ [27,32,47] (up to a log factor [48]).

With figures 7 and 8, we demonstrate numerical simulations that accurately capture the heterogeneous engineering scale response of the two kirigami patterns under complex boundary conditions. We consider, in particular, three boundary conditions: pulling along diagonal line (figures 7 and 8*a*), pulling along centreline (figures 7 and 8*b*), and pulling a centre point with the opposite corner points fixed (figures 7 and 8*c*). Each such loading leads to a soft response in the two experimental patterns, far from any pure mechanism.

Some general features emerge from the experiments. In the rotating-squares sample, slit actuation quickly decays in arcs around the loading points. In the hyperbolic sample, slit actuation instead radiates from the loaded boundary, yielding large bands of actuation within the sample's bulk. This 'decay versus persistence' in actuation affirms the link to Poisson's ratio derived in [47] and discussed in §3c and §5a. Our simulations capture these general features, as well as finer details.

With the moduli parameters of the model given by equation (5.3), we carry out simulations by matching the boundary conditions of the three experiments for each sample. (These boundary conditions include the displacements where the sample is loaded, as well as the natural traction-free and ξ boundary conditions in equation (4.4)). The simulations are shown on the bottom row of figure 7 and figure 8, and each recovers the pattern's engineering scale response on the top row. As the figures highlight, the solved-for slit actuation agrees qualitatively with that of the experiments. Table 1 also compares various metrics of the normed difference in boundary

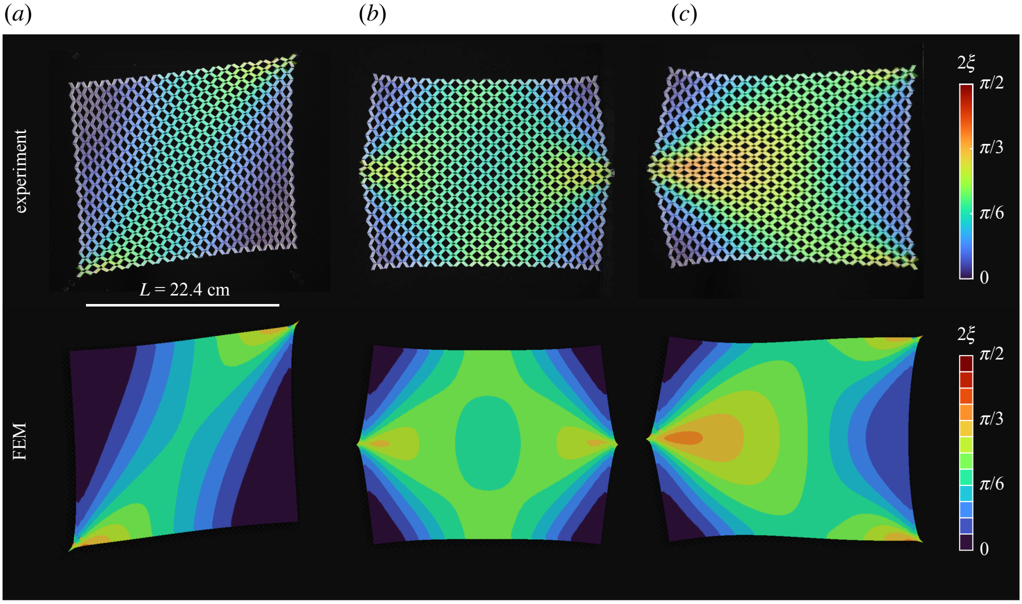

Figure 8. Experiments and simulations of the hyperbolic sample. Three boundary conditions are applied: (*a*) pulling along diagonal line; (*b*) pulling along centreline; (*c*) pulling a centre point with opposite corner points fixed. L is the undeformed sample length. Colour maps show the slit actuation angle ξ, extracted from the experiment per appendix B.

Table 1. Comparison of the normed difference of boundary displacements between experimental and simulated samples. Three metrics of this boundary value comparison are shown: the root mean squared deviation, the max, and the mean. Each is normalized by the unit cell length ℓ from figure 5, which is 1.4 cm for all experimental samples.

boundary displacement comparison	RMS$/\ell$	Max$/\ell$	Mean$/\ell$
rotating-squares, figure 7*a*	0.16	0.33	0.15
rotating-squares, figure 7*b*	0.13	0.28	0.12
rotating-squares, figure 7*c*	0.27	0.45	0.26
hyperbolic, figure 8*a*	0.24	0.36	0.22
hyperbolic, figure 8*b*	0.11	0.20	0.10
hyperbolic, figure 8*c*	0.25	0.38	0.23

displacement between the experimental and simulation results. The agreement is quantitatively excellent. Each pattern is subject to roughly 10–30% engineering strain, yet the boundary discrepancies are but a fraction of the length of a unit cell.

(d) Force–displacement curves

As a final demonstration of the capabilities of our model, we compare an experimental force–displacement curve to analogous simulations. We focus on the rotating squares architecture and the centre-pulling loading condition for the demonstration. The experimental sample, introduced in figure 5*a*, is loaded along its centreline using a string and weights, as illustrated in figure 9*a*. For each value of applied force, the total stretch of the specimen along the same centreline is recorded via image processing. Additional details on the experimental set-up are reported in appendix B.

The loading and unloading experimental curves are plotted in red in figure 9*b*, where the solid line indicates the average and the shaded area encompasses the standard deviation from

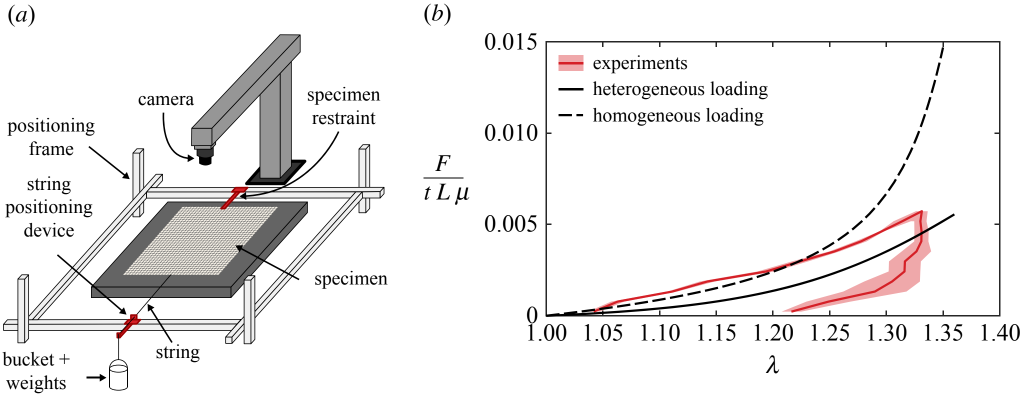

Figure 9. (*a*) Schematic of our experimental setup for force–displacement measurement. The specimen rests on a smooth surface and is restrained using fixtures connected to an outer frame. Forces are applied to the specimen (here, at a point where the centreline meets the boundary) through strings and weights. (*b*) Normalized force as a function of the centreline stretch λ. The experimental data is red, with the continuous line giving the average of three measurements and the shaded area showing the standard deviation. The solid black curve is the theoretical curve found by simulating the effective model. For comparison, the dashed curve shows the theoretical response to uniform loading, using the same fitting parameters.

three tests. In the plot, the force is non-dimensionalized by the thickness of the sample $t = 0.15\,\mathrm{cm}$, its width $L = 22.4\,\mathrm{cm}$ and the shear modulus of the material $\mu = 0.38\,\mathrm{MPa}$ (obtained from experimental data on the behaviour of natural rubber gum in [53]). Friction clearly plays a role in the experiment. While the sample remains elastic throughout the entire loading and unloading process, friction causes stretches to be smaller than in a frictionless case during loading, and larger during unloading. Despite this behaviour, it is still illuminating to compare this experiment to simulations of our effective (and frictionless) model.

The black curve in figure 9*b* plots the simulated force–displacement curve for the heterogeneous loading shown in the bottom pane of figure 7*b* (the centre-pulling case). The simulation is carried out using the rotating squares parameters $\alpha, \beta, c_1/c_0, c_2/c_0$ fitted previously. The modulus c_0, which has yet to be prescribed, acts as an effective shear modulus that sets the overall magnitude of the force but does not affect the shape of the curve. We choose it as $c_0 = \mu/3.5$ so that the simulated curve is approximately in the middle of the loading and unloading experimental curve. This prescription is an attempt to capture the frictionless behaviour of the sample, which should fall somewhere within the width of the hysteresis loop. We note that the simulated sample is displacement-controlled rather than force-controlled (the former is easier to implement in our Abaqus UEL). Its forces are computed using a version of Castigliano's method described in appendix C. We expect an analogous force-controlled simulation to produce the same force–displacement curve.

The experimental and simulated curves exhibit the same trends and are quantitatively consistent. Both are nonlinear and convex, and the modulus used in the model ($c_0 = \mu/3.5$) is physically reasonable. In the simulation, the forces emerge from stresses due to the nonlinear bulk elastic term at a given applied displacement. This term attempts to relax some of the actuation ξ of the linear hinge bending term. However, there is geometric frustration in this process; the effective deformation and slit actuation must approximate a local mechanism via equation (3.1). This frustration increases as the boundary displacement increases, leading to the convex nature of the curve. That the experimental curve displays a similar convex profile is another demonstration of the quality of our generalized continuum model.

Adding to the discussion, the dashed black line in figure 9*b* plots the analytical force–displacement curve for the uniform stretch case described in §5b using the same parameters as the simulation. Compared to the centre-pulling case, the curve has a larger value of force at each given stretch, which is expected since much more of the boundary is loaded at the same value of stretch. The curve also increases dramatically at high values of stretch, where the entire pattern has begun to exhaust its soft mechanistic response. At this stage, the hinges must stretch as well as bend, which fully engages the bulk elastic term in the model. Interestingly, the same level of actuation in the centre-pulling case—actuation warranting significant hinge stretching—only occurs in localized regions near the loading location. This feature appears to delay the inevitable sharp change in the overall force response.

6. Conclusion

This paper modelled the class of planar, rhombi-slit kirigami metamaterials as generalized elastic continua. We first described how to obtain the cell-averaged response of the pattern's mechanism deformations. Then we formulated an elastic energy that drove the pattern's effective deformation and slit actuation towards this cell-averaged response locally, and treated the slit actuation as an auxiliary field variable to account for additional physically relevant sources of elasticity. Through implementation in Abaqus, we demonstrated a model capable of predicting the response of kirigami metamaterials across designs and loading conditions.

Although we only discussed a specific energy formula for a specific family of kirigami, our method can be generalized to a wide range of kirigami metamaterials. For instance, by modifying the shape tensor in equation (2.4), we can model planar kirigami with parallelogram slits [47], and presumably any other periodic and planar kirigami with periodic mechanisms to be discovered. We can also account for spatial variations of unit cell design, as in [53], by allowing the design parameters in the model to vary. Finally, while our constitutive choices in equations (3.3) and (3.4) were simple by design, they can be easily updated to enrich the model to account for more nuanced features of the kirigami's response than those discussed here.

Taking a broader view, our results suggest that modelling mechanical metamaterials as generalized elastic continua is a powerful approach to understanding their nonlinear response—one potentially capable of efficiently navigating the design space of these materials, while remaining predictive under a wide range of loads. By focusing on rhombi-slit kirigami, we took a purposefully concrete and simple approach to modelling. We hope this choice makes our work widely accessible and paves the way for broad generalization going forward.

Ethics. This work did not involve any active collection of human or animal data.

Data accessibility. The Abaqus UEL codes are available on GitHub at: https://github.com/yzheng29/kirigami-metamaterial_UEL.

Authors' contributions. Y.Z.: conceptualization, formal analysis, investigation, methodology, software, writing—original draft; I.N.: investigation; I.T.: conceptualization, methodology, writing—review and editing; P.C.: conceptualization, investigation, visualization, writing—review and editing; P.P.: conceptualization, methodology, supervision, writing—original draft.

All authors gave final approval for publication and agreed to be held accountable for the work performed therein.

Conflict of interest declaration. We declare we have no competing interests.

Funding. Y.Z. and P.P. acknowledge support through P.P.'s startup package at the University of Southern California. I.T. acknowledges support from the National Science Foundation (DMS-CAREER-2145225). P.C. and I.N. acknowledge support from the National Science Foundation (CMMI-2045191).

Disclaimer. The information provided in this paper is the sole opinion of the authors and does not necessarily reflect the views of the sponsoring agencies.

Appendix A. Explicit tangent formulas for Abaqus FEM implementation

Here, we develop explicit formulae for the tangents in equation (4.10) to complete the description of the FEM formulation for Abaqus implementation. The formulae reference functions introduced in §§3 and 4 which we do not repeat here. They also make use of shape functions defined on the current configuration $\tilde{N}^A : \mathbf{y}_{\text{eff}}(\Omega) \to \mathbb{R}$ via $\tilde{N}^A \circ \mathbf{y}_{\text{eff}}(\mathbf{x}) = N^A(\mathbf{x})$, for which the gradients transform as

$$\nabla\tilde{N}^A \circ \mathbf{y}_{\mathrm{eff}}(\mathbf{x}) = (\tilde{\mathbf{F}}(\mathbf{x},\mathbf{u}))^{-T}\nabla N^A(\mathbf{x}). \tag{A 1}$$

This transformation is a convenient way of bringing out certain symmetries in the parts of these tangents associated with the bulk elastic term W_0. ([49, ch 8.4] has a detailed exposition on hyperelastic tangent formulae, where this transformation is employed.) In brief, we find that

$$\begin{aligned}
[\mathbf{K}^{AB}_{\mathrm{disp}}(\mathbf{u},\boldsymbol{\xi})]_{ab} &= \int_\Omega \{[\mathbb{C}_{\mathrm{disp}}(\tilde{\mathbf{F}}(\mathbf{x},\mathbf{u})\mathbf{A}^{-1}(\tilde{\theta}(\mathbf{x},\boldsymbol{\xi})))]_{abcd}[\nabla\tilde{N}^A \circ \mathbf{y}_{\mathrm{eff}}(\mathbf{x})]_c[\nabla\tilde{N}^B \circ \mathbf{y}_{\mathrm{eff}}(\mathbf{x})]_d\}\,\mathrm{d}A,\\
[\mathbf{k}^{AB}_{\mathrm{disp}}(\mathbf{u},\boldsymbol{\xi})]_a = [\mathbf{k}^{BA}_{\mathrm{act}}(\mathbf{u},\boldsymbol{\xi})]_a &= \int_\Omega \{[\mathbf{C}_{\mathrm{mix}}(\tilde{\mathbf{F}}(\mathbf{x},\mathbf{u}),\tilde{\theta}(\mathbf{x},\boldsymbol{\xi}))]_{ab}[\nabla\tilde{N}^B \circ \mathbf{y}_{\mathrm{eff}}(\mathbf{x})]_b N^A(\mathbf{x})\}\,\mathrm{d}A,\\
k^{AB}_{\mathrm{act}}(\mathbf{u},\boldsymbol{\xi}) &= \int_\Omega \left\{\frac{\partial}{\partial\theta}[f_{\mathrm{act}}(\tilde{\mathbf{F}}(\mathbf{x},\mathbf{u}),\tilde{\theta}(\mathbf{x},\boldsymbol{\xi}))]N^A(\mathbf{x})N^B(\mathbf{x}) + 2c_2\nabla N^A(\mathbf{x})\cdot\nabla N^B(\mathbf{x})\right\}\mathrm{d}A
\end{aligned} \tag{A 2}$$

in two-dimensional index notation with repeated indices summed. The moduli in these formulae are associated with partial derivatives of $W(\mathbf{F},\theta,\mathbf{p})$. Structurally, they are of the form

$$\begin{aligned}
[\mathbb{C}_{\mathrm{disp}}(\mathbf{G})]_{abcd} &= \left[\frac{\partial\boldsymbol{\tau}_0(\mathbf{G})}{\partial\mathbf{G}}\right]_{bdal}[\mathbf{G}]_{cl} - [\boldsymbol{\tau}_0(\mathbf{G})]_{bc}[\mathbf{I}]_{ad},\\
\mathbf{C}_{\mathrm{mix}}(\mathbf{F},\theta) &:= \widetilde{\mathbf{C}}_{\mathrm{mix}}(\mathbf{F}\mathbf{A}^{-1}(\theta),\mathbf{A}'(\theta)\mathbf{A}^{-1}(\theta)),\\
\widetilde{\mathbf{C}}_{\mathrm{mix}}(\mathbf{G},\mathbf{H}) &:= -\frac{\partial\boldsymbol{\tau}_0(\mathbf{G})}{\partial\mathbf{G}} : (\mathbf{G}\mathbf{H}),\\
\frac{\partial}{\partial\theta}f_{\mathrm{act}}(\mathbf{F},\theta) &= -\frac{\mathrm{d}}{\mathrm{d}\theta}[\mathbf{P}_0(\mathbf{G}(\theta)) : (\mathbf{G}(\theta)\mathbf{H}(\theta))] + 2c_1\\
&=: c_{\mathrm{act}}(\mathbf{G}(\theta),\mathbf{H}(\theta),\mathbf{H}'(\theta)),
\end{aligned} \tag{A 3}$$

where the arguments of $c_{\mathrm{act}}(\cdot)$ are defined as $\mathbf{G}(\theta) := \mathbf{F}\mathbf{A}^{-1}(\theta)$ and $\mathbf{H}(\theta) := \mathbf{A}'(\theta)\mathbf{A}^{-1}(\theta)$. Each moduli can also be expressed in terms of elementary functions as

$$\begin{aligned}
[\mathbb{C}_{\mathrm{disp}}(\mathbf{G})]_{abcd} &= \frac{2c_0}{J_{\mathbf{G}}}\{[\mathbf{I}]_{ba}[\mathbf{G}\mathbf{G}^{\mathrm{T}}]_{dc} - [\mathbf{G}\mathbf{G}^{\mathrm{T}}]_{bd}[\mathbf{I}]_{ac}\\
&\quad - [\mathbf{I}]_{bd}[\mathbf{G}\mathbf{G}^{\mathrm{T}}]_{ac} + (2J^3_{\mathbf{G}} - J^2_{\mathbf{G}})[\mathbf{I}]_{bd}[\mathbf{I}]_{ac}\}\\
&\quad + \frac{2c_0}{J_{\mathbf{G}}}\left\{-(J^3_{\mathbf{G}} - J^2_{\mathbf{G}})[\mathbf{I}]_{bc}[\mathbf{I}]_{ad} + \frac{1}{2}|\mathbf{G}|^2([\mathbf{I}]_{bd}[\mathbf{I}]_{ac} + [\mathbf{I}]_{bc}[\mathbf{I}]_{ad})\right\},\\
\widetilde{\mathbf{C}}_{\mathrm{mix}}(\mathbf{G},\mathbf{H}) &= -\frac{2c_0}{J_{\mathbf{G}}}(2\,\mathrm{sym}(\mathbf{G}\mathbf{H}\mathbf{G}^{\mathrm{T}}) - \mathrm{Tr}(\mathbf{G}\mathbf{H}\mathbf{G}^{\mathrm{T}})\mathbf{I}\\
&\quad + \mathrm{Tr}(\mathbf{H})\left\{\left(\frac{1}{2}|\mathbf{G}|^2 + 2J^3_{\mathbf{G}} - J^2_{\mathbf{G}}\right)\mathbf{I} - \mathbf{G}\mathbf{G}^{\mathrm{T}}\right\}\Bigg),\\
c_{\mathrm{act}}(\mathbf{G},\mathbf{H},\mathbf{M}) &= \frac{2c_0}{J_{\mathbf{G}}}(|\mathbf{G}\mathbf{H}|^2 + \mathrm{Tr}(\mathbf{G}(\mathbf{H}^2 - \mathbf{M})\mathbf{G}^{\mathrm{T}}) - 2\,\mathrm{Tr}(\mathbf{G}\mathbf{H}\mathbf{G}^{\mathrm{T}})\,\mathrm{Tr}(\mathbf{H}))\\
&\quad + \frac{2c_0}{J_{\mathbf{G}}}\Bigg(\left\{2J^3_{\mathbf{G}} - J^2_{\mathbf{G}} + \frac{1}{2}|\mathbf{G}|^2\right\}(\mathrm{Tr}(\mathbf{H}))^2\\
&\quad + \left\{\frac{1}{2}|\mathbf{G}|^2 - J^3_{\mathbf{G}} + J^2_{\mathbf{G}}\right\}\mathrm{Tr}(\mathbf{M})\Bigg) + 2c_1,
\end{aligned} \tag{A 4}$$

where sym(·) denotes the symmetric part of a square matrix.

Appendix B. Materials and methods

We cut the kirigami specimens out of 1.5 mm-thick natural rubber sheets (McMaster-Carr 8633K71) using an 80 Watt Epilog Fusion Pro 32 laser cutter. During the fabrication, the laser cutter is focused on the bottom face of the rubber sheet to avoid burning the specimens and to produce clean cuts. The specimens are painted with white primer paint to create high contrast with a black background, which facilitates image processing. Images of the samples are recorded by means of a FLIR 5-megapixel 35 fps camera with Edmund Optics lenses.

Our method for characterizing the slit actuation in the deformed experimental samples is similar to our previous work [47] and to that of others [28]. We obtain quantitative information on the deformation through digital image processing in MATLAB. After converting the images to binary (using the `imbinarize` function), we obtain the centroid $\mathbf{c}^{(i,j)}$, semi-major axis $\mathbf{a}^{(i,j)}$ and semi-minor axis $\mathbf{b}^{(i,j)}$ of the central slit of each (i,j)-cell using the `regionprops` function. Then, using $d = \ell/20$ from §5a and ξ_0 from figure 5*c*,*d*, we calculate $\xi^{(i,j)}$ from $\tan(\xi^{(i,j)} + \xi_0) = (|\mathbf{a}^{(i,j)}| + d/2)/(|\mathbf{b}^{(i,j)}| + d/2)$ and take $\gamma^{(i,j)}$ as the inclination of the major axis with respect to the horizontal. Since we know the dimensions of the panels in the sample, we overlay a ξ colour map of each idealized deformed unit cell (with angles $(\xi^{(i,j)}, \gamma^{(i,j)})$) onto the experimental pattern, centred at the slit centroid $\mathbf{c}^{(i,j)}$.

The force–displacement data are obtained with the setup illustrated in figure 9*a*. The specimen rests on a smooth surface (Slippery UHMW Polyethylene). For anchoring and positioning purposes, we build a frame of T-slotted rails and use a three-dimensionally-printed hook to pin down the specimen onto the surface. At the desired loading location, we tie a nylon string to the specimen. The string then passes through a three-dimensionally-printed positioning device tied to the frame, and is connected to a bucket. We add known weights to the bucket and calculate the force that the weights impart onto the specimen. These experiments are force-controlled: we apply a weight and measure the specimen's stretch along a desired direction. The stretch is measured with the same camera mentioned previously in this section. The deformed length of the specimen is measured through an automated pixel counting process in MATLAB.

Appendix C. Castigliano's method to obtain forces

The theoretical forces in figure 9 are calculated by differentiating the equilibrium energy with respect to the overall displacement, using our generalized elastic continuum model. This is essentially Castigliano's method from structural mechanics. Here, we give a brief justification of this approach.

We assume that the effective reference domain of the kirigami pattern is $\Omega = (-L/2, L/2)^2$ and focus on the centre-pulling case, where the pattern's effective deformation $\mathbf{y}_{\text{eff}}(\mathbf{x})$ and slit actuation $\xi(\mathbf{x})$ solve the equilibrium equations in equation (4.3) subject to the boundary conditions

$$\begin{cases} \mathbf{y}_{\text{eff}}(\mathbf{x}) = \mathbf{x} \pm \frac{q}{2}\mathbf{e}_1 & \text{for } \mathbf{x}\cdot\mathbf{e}_1 = \pm L/2, \mathbf{x}\cdot\mathbf{e}_2 \in (-\epsilon, \epsilon) \\ \mathbf{P}_{\mathbf{y}_{\text{eff}},\xi}(\mathbf{x})\mathbf{n}_R(\mathbf{x}) = \mathbf{0} & \text{on the rest of the boundary } \partial\Omega \\ \nabla\xi(\mathbf{x})\cdot\mathbf{n}_R(\mathbf{x}) = 0 & \text{on all of } \partial\Omega. \end{cases} \tag{C 1}$$

The parameter $\epsilon > 0$ idealizes the width where the sample is gripped and displaced on centre-pulling. The parameter $q \geq 0$ is the overall displacement of the horizontal centreline as the sample is monotonically loaded. It starts at the value $q = 0$ and increases monotonically to achieve a maximum stretch $\lambda = 1 + q/L \approx 1.35$ in both the simulation and experiment in figure 9. Of course, $\mathbf{y}_{\text{eff}}$ and ξ depend on q.

As in Castigliano's method, we differentiate the equilibrium value of the generalized elastic continuum energy

$$\mathcal{U}(q) := t\int_{\Omega} W(\nabla\mathbf{y}_{\text{eff}}(\mathbf{x}), \xi(\mathbf{x}), \nabla\xi(\mathbf{x}))\,\mathrm{d}A \tag{C 2}$$

with respect to the overall displacement q. Note $t > 0$ is the thickness of the sample. Passing the derivative under the integral sign and using the definitions from §§3 and 4, there follows:

$$\begin{aligned} \frac{\mathrm{d}\mathcal{U}}{\mathrm{d}q} = t\int_{\Omega} \bigg\{ & \mathbf{P}_{\mathbf{y}_{\text{eff}},\xi}(\mathbf{x}) : \nabla\left(\frac{\partial\mathbf{y}_{\text{eff}}(\mathbf{x})}{\partial q}\right) + f_{\text{act}}(\nabla\mathbf{y}_{\text{eff}}(\mathbf{x}), \xi(\mathbf{x}))\frac{\partial\xi(\mathbf{x})}{\partial q} \\ & + 2c_2\nabla\xi(\mathbf{x})\cdot\nabla\left(\frac{\partial\xi(\mathbf{x})}{\partial q}\right)\bigg\}\,\mathrm{d}A. \end{aligned} \tag{C 3}$$

By the divergence theorem,

$$\begin{aligned}\frac{\mathrm{d}\mathcal{U}}{\mathrm{d}q} = t\int_{\Omega} \bigg\{&-(\nabla\cdot \mathbf{P}^{\mathrm{T}}_{\mathbf{y}_{\mathrm{eff}},\xi}(\mathbf{x}))\cdot \frac{\partial \mathbf{y}_{\mathrm{eff}}(\mathbf{x})}{\partial q}\\ &+ (f_{\mathrm{act}}(\nabla\mathbf{y}_{\mathrm{eff}}(\mathbf{x}),\xi(\mathbf{x})) - 2c_2\nabla^2\xi(\mathbf{x}))\frac{\partial\xi(\mathbf{x})}{\partial q}\bigg\}\,\mathrm{d}A\\ &+ t\int_{\partial\Omega}\bigg\{(\mathbf{P}_{\mathbf{y}_{\mathrm{eff}},\xi}(\mathbf{x})\mathbf{n}_R(\mathbf{x}))\cdot\frac{\partial \mathbf{y}_{\mathrm{eff}}(\mathbf{x})}{\partial q} + (2c_2\nabla\xi(\mathbf{x})\cdot\mathbf{n}_R(\mathbf{x}))\frac{\partial \xi(\mathbf{x})}{\partial q}\bigg\}\,\mathrm{d}\Gamma.\end{aligned} \tag{C 4}$$

The equilibrium equations in equation (4.3) imply that the first integral above vanishes. Concerning the second, let $\mathbf{x}^{\pm}(s) = \pm(L/2)\mathbf{e}_1 + s\mathbf{e}_2$ parametrize the boundaries of the applied displacement. By the boundary conditions in equation (C 1),

$$\begin{aligned}\frac{\mathrm{d}\mathcal{U}}{\mathrm{d}q} &= t\int_{-\epsilon}^{\epsilon}\bigg\{\mathbf{P}_{\mathbf{y}_{\mathrm{eff}},\xi}(\mathbf{x}^{+}(s))\mathbf{e}_1\cdot\frac{\partial}{\partial q}\left(\mathbf{x}^{+}(s)+\frac{q}{2}\mathbf{e}_1\right)\\ &\qquad -\mathbf{P}_{\mathbf{y}_{\mathrm{eff}},\xi}(\mathbf{x}^{-}(s))\mathbf{e}_1\cdot\frac{\partial}{\partial q}\left(\mathbf{x}^{-}(s)-\frac{q}{2}\mathbf{e}_1\right)\bigg\}\,\mathrm{d}s\\ &= \underbrace{\frac{t}{2}\int_{-\epsilon}^{\epsilon}\mathbf{e}_1\cdot\mathbf{P}_{\mathbf{y}_{\mathrm{eff}},\xi}(\mathbf{x}^{+}(s))\mathbf{e}_1\,\mathrm{d}s}_{:=(1/2)f^{+}} + \underbrace{\frac{t}{2}\int_{-\epsilon}^{\epsilon}\mathbf{e}_1\cdot\mathbf{P}_{\mathbf{y}_{\mathrm{eff}},\xi}(\mathbf{x}^{-}(s))\mathbf{e}_1\,\mathrm{d}s}_{:=(1/2)f^{-}}.\end{aligned} \tag{C 5}$$

The terms f^{+} and f^{-} give the tensile force applied to the right and left boundary, respectively. As these are equal by force balance, i.e. $f^{+} = f^{-} = F$, we conclude that

$$\frac{\mathrm{d}\mathcal{U}}{\mathrm{d}q} = F. \tag{C 6}$$

In summary, the force in the centre-pulling set-up can be found by differentiating the equilibrium energy with respect to the overall displacement. equation (C 6) also holds for the homogeneous set-up in figure 9. The justification of this result is similar and is left to the reader.

References

1. Schenk M, Guest SD. 2013 Geometry of Miura-folded metamaterials. *Proc. Natl Acad. Sci. USA* **110**, 3276–3281. (doi:10.1073/pnas.1217998110)
2. Grima JN, Evans KE. 2000 Auxetic behavior from rotating squares. *J. Mater. Sci. Lett.* **19**, 1563–1565. (doi:10.1023/A:1006781224002)
3. Lubensky TC, Kane CL, Mao X, Souslov A, Sun K. 2015 Phonons and elasticity in critically coordinated lattices. *Rep. Prog. Phys.* **78**, 073901. (doi:10.1088/0034-4885/78/7/073901)
4. Bertoldi K, Vitelli V, Christensen J, Van Hecke M. 2017 Flexible mechanical metamaterials. *Nat. Rev. Mater.* **2**, 1–11. (doi:10.1038/natrevmats.2017.66)
5. Liu H, Plucinsky P, Feng F, Soor A, James RD. 2022 Origami and the structure of materials. *SIAM News* **55**, 1–6.
6. Kuribayashi K, Tsuchiya K, You Z, Tomus D, Umemoto M, Ito T, Sasaki M. 2006 Self-deployable origami stent grafts as a biomedical application of Ni-rich TiNi shape memory alloy foil. *Mater. Sci. Eng. A* **419**, 131–137. (doi:10.1016/j.msea.2005.12.016)
7. Velvaluri P, Soor A, Plucinsky P, de Miranda RL, James RD, Quandt E. 2021 Origami-inspired thin-film shape memory alloy devices. *Sci. Rep.* **11**, 10988. (doi:10.1038/s41598-021-90217-3)
8. Shintake J, Cacucciolo V, Floreano D, Shea H. 2018 Soft robotic grippers. *Adv. Mater.* **30**, 1707035. (doi:10.1002/adma.201707035)
9. Rafsanjani A, Bertoldi K, Studart AR. 2019 Programming soft robots with flexible mechanical metamaterials. *Sci. Rob.* **4**, eaav7874. (doi:10.1126/scirobotics.aav7874)
10. Miura K. 1985 Method of packaging and deployment of large membranes in space. *Inst. Space Astronaut. Sci. Rep.* **618**, 1–9.
11. Arya M, Lee N, Pellegrino S. 2017 Crease-free biaxial packaging of thick membranes with slipping folds. *Int. J. Solids Struct.* **108**, 24–39. (doi:10.1016/j.ijsolstr.2016.08.013)

12. Huffman DA. 1976 Curvature and creases: a primer on paper. *IEEE Trans. Comput.* **25**, 1010–1019. (doi:10.1109/TC.1976.1674542)
13. Belcastro S-M, Hull TC. 2002 Modelling the folding of paper into three dimensions using affine transformations. *Linear Algebra Appl.* **348**, 273–282. (doi:10.1016/S0024-3795(01)00608-5)
14. Tachi T. 2009 Generalization of rigid-foldable quadrilateral-mesh origami. *J. Int. Assoc. Shell Spat. Struct.* **50**, 173–179.
15. Chen Y, Feng H, Ma J, Peng R, You Z. 2016 Symmetric waterbomb origami. *Proc. R. Soc. A* **472**, 20150846. (doi:10.1098/rspa.2015.0846)
16. Lang RJ, Howell L. 2018 Rigidly foldable quadrilateral meshes from angle arrays. *J. Mech. Rob.* **10**, 021004. (doi:10.1115/1.4038972)
17. Feng F, Dang X, James RD, Plucinsky P. 2020 The designs and deformations of rigidly and flat-foldable quadrilateral mesh origami. *J. Mech. Phys. Solids* **142**, 104018. (doi:10.1016/j.jmps.2020.104018)
18. Dieleman P, Vasmel N, Waitukaitis S, van Hecke M. 2020 Jigsaw puzzle design of pluripotent origami. *Nat. Phys.* **16**, 63–68. (doi:10.1038/s41567-019-0677-3)
19. Dudte LH, Choi GPT, Mahadevan L. 2021 An additive algorithm for origami design. *Proc. Natl Acad. Sci. USA* **118**, e2019241118. (doi:10.1073/pnas.2019241118)
20. Choi GPT, Dudte LH, Mahadevan L. 2021 Compact reconfigurable kirigami. *Phys. Rev. Res.* **3**, 043030. (doi:10.1103/PhysRevResearch.3.043030)
21. Dang X, Feng F, Duan H, Wang J. 2022 Theorem on the compatibility of spherical kirigami tessellations. *Phys. Rev. Lett.* **128**, 035501. (doi:10.1103/PhysRevLett.128.035501)
22. Walker A, Stankovic T. 2022 Algorithmic design of origami mechanisms and tessellations. *Commun. Mater.* **3**, 4. (doi:10.1038/s43246-022-00227-5)
23. Pellegrino S, Calladine CR. 1986 Matrix analysis of statically and kinematically indeterminate frameworks. *Int. J. Solids Struct.* **22**, 409–428. (doi:10.1016/0020-7683(86)90014-4)
24. Schenk M, Guest SD. 2011 Origami folding: a structural engineering approach. *Origami* **5**, 291–304.
25. Filipov ET, Liu K, Tachi T, Schenk M, Paulino GH. 2017 Bar and hinge models for scalable analysis of origami. *Int. J. Solids Struct.* **124**, 26–45. (doi:10.1016/j.ijsolstr.2017.05.028)
26. Liu K, Paulino GH. 2017 Nonlinear mechanics of non-rigid origami: an efficient computational approach. *Proc. R. Soc. A* **473**, 20170348. (doi:10.1098/rspa.2017.0348)
27. Coulais C, Kettenis C, van Hecke M. 2018 A characteristic length scale causes anomalous size effects and boundary programmability in mechanical metamaterials. *Nat. Phys.* **14**, 40–44. (doi:10.1038/nphys4269)
28. Deng B, Yu S, Forte AE, Tournat V, Bertoldi K. 2020 Characterization, stability, and application of domain walls in flexible mechanical metamaterials. *Proc. Natl Acad. Sci. USA* **117**, 31 002–31 009. (doi:10.1073/pnas.2015847117)
29. Wei ZY, Guo ZV, Dudte L, Liang HY, Mahadevan L. 2013 Geometric mechanics of periodic pleated origami. *Phys. Rev. Lett.* **110**, 215501. (doi:10.1103/PhysRevLett.110.215501)
30. Nassar H, Lebée A, Monasse L. 2017 Curvature, metric and parametrization of origami tessellations: theory and application to the eggbox pattern. *Proc. R. Soc. A* **473**, 20160705. (doi:10.1098/rspa.2016.0705)
31. Khajehtourian R, Kochmann DM. 2021 A continuum description of substrate-free dissipative reconfigurable metamaterials. *J. Mech. Phys. Solids* **147**, 104217. (doi:10.1016/j.jmps.2020.104217)
32. Czajkowski M, Coulais C, van Hecke M, Rocklin D. 2022 Conformal elasticity of mechanism-based metamaterials. *Nat. Commun.* **13**, 221. (doi:10.1038/s41467-021-27825-0)
33. Nassar H, Lebée A, Werner E. 2022 Strain compatibility and gradient elasticity in morphing origami metamaterials. *Extreme Mech. Lett.* **53**, 101722. (doi:10.1016/j.eml.2022.101722)
34. McMahan C, Akerson A, Celli P, Audoly B, Daraio C. 2022 Effective continuum models for the buckling of non-periodic architected sheets that display quasi-mechanism behaviors. *J. Mech. Phys. Solids* **166**, 104934. (doi:10.1016/j.jmps.2022.104934)
35. McInerney J, Paulino GH, Rocklin D. 2021 Discrete symmetries control mechanical response in parallelogram-based origami. Preprint (https://arxiv.org/abs/2108.05825).
36. Brown WF. 1966 *Magnetoelastic interactions*, vol. **9**. Berlin, Germany: Springer.
37. Toledano P, Toledano J-C. 1987 *Landau theory of phase transitions, the: application to structural, incommensurate, magnetic and liquid crystal systems*, vol. 3. Singapore: World Scientific Publishing Company.

38. Bhattacharya K. 2003 *Microstructure of martensite: why it forms and how it gives rise to the shape-memory effect*, vol. 2. Oxford, UK: Oxford University Press.
39. Eringen AC. 2012 *Microcontinuum field theories: I. Foundations and solids*. Singapore: Springer Science & Business Media.
40. Saremi A, Rocklin Z. 2020 Topological elasticity of flexible structures. *Phys. Rev. X* **10**, 011052.
41. Nassar H, Chen H, Huang G. 2020 Microtwist elasticity: a continuum approach to zero modes and topological polarization in Kagome lattices. *J. Mech. Phys. Solids* **144**, 104107. (doi:10.1016/j.jmps.2020.104107)
42. Lakes RS. 2022 Extremal hinged lattices do not obey the theory of elasticity. *Z. Angew. Math. Phys.* **73**, 27. (doi:10.1007/s00033-021-01664-x)
43. Alibert J-J, Seppecher P, Dell'Isola F. 2003 Truss modular beams with deformation energy depending on higher displacement gradients. *Math. Mech. Solids* **8**, 51–73. (doi:10.1177/1081286503008001658)
44. Abdoul-Anziz H, Seppecher P. 2018 Strain gradient and generalized continua obtained by homogenizing frame lattices. *Math. Mech. Complex Syst.* **6**, 213–250. (doi:10.2140/memocs.2018.6.213)
45. Seppecher P *et al.* 2019 Pantographic metamaterials: an example of mathematically driven design and of its technological challenges. *Continuum Mech. Thermodyn.* **31**, 851–884.
46. Durand B, Lebée A, Seppecher P, Sab K. 2022 Predictive strain-gradient homogenization of a pantographic material with compliant junctions. *J. Mech. Phys. Solids* **160**, 104773. (doi:10.1016/j.jmps.2021.104773)
47. Zheng Y, Niloy I, Celli P, Tobasco I, Plucinsky P. 2022 Continuum field theory for the deformations of planar kirigami. *Phys. Rev. Lett.* **128**, 208003. (doi:10.1103/PhysRevLett.128.208003)
48. Plucinsky P, Zheng Y, Celli P, Tobasco I. In preparation. Derivation of a mechanism gradient elastic theory for planar kirigami.
49. Bower AF. 2009 *Applied mechanics of solids*. Boca Raton, FL: CRC press.
50. Do Carmo MP. 2016 *Differential geometry of curves and surfaces: revised and updated*, 2nd edn. New York, NY: Courier Dover Publications.
51. Courant R, Hilbert D. 2008 *Methods of mathematical physics: partial differential equations*. New York, NY: John Wiley & Sons.
52. Smith M. 2009 *ABAQUS/standard user's manual, version 6.9*. USA: Dassault Systèmes Simulia Corp.
53. Celli P, McMahan C, Ramirez B, Bauhofer A, Naify C, Hofmann D, Audoly B, Daraio C. 2018 Shape-morphing architected sheets with non-periodic cut patterns. *Soft Matter* **14**, 9744–9749. (doi:10.1039/C8SM02082E)